ADVANCED MATERIALS
www.advmat.de

Highly Efficient Nitrogen-Fixing Microbial Hydrogel Device for Sustainable Solar Hydrogen Production

Wang Hee Lee, Chang-Kyu Yoon, Hyunseo Park, Ga-Hee Park, Jae Hwan Jeong, Gi Doo Cha, Byoung-Hoon Lee, Juri Lee, Chan Woo Lee, Megalamane S. Bootharaju, Sung-Hyuk Sunwoo, Jaeyune Ryu, Changha Lee, Yong-Joon Cho, Tae-Wook Nam, Kyung Hyun Ahn, Taeghwan Hyeon, Yeong-Jae Seok,* and Dae-Hyeong Kim**

Conversion of sunlight and organic carbon substrates to sustainable energy sources through microbial metabolism has great potential for the renewable energy industry. Despite recent progress in microbial photosynthesis, the development of microbial platforms that warrant efficient and scalable fuel production remains in its infancy. Efficient transfer and retrieval of gaseous reactants and products to and from microbes are particular hurdles. Here, inspired by water lily leaves floating on water, a microbial device designed to operate at the air–water interface and facilitate concomitant supply of gaseous reactants, smooth capture of gaseous products, and efficient sunlight delivery is presented. The floatable device carrying *Rhodopseudomonas parapalustris*, of which nitrogen fixation activity is first determined through this study, exhibits a hydrogen production rate of 104 mmol h^{-1} m^{-2}, which is 53 times higher than that of a conventional device placed at a depth of 2 cm in the medium. Furthermore, a scaled-up device with an area of 144 cm^2 generates hydrogen at a high rate of 1.52 L h^{-1} m^{-2}. Efficient nitrogen fixation and hydrogen generation, low fabrication cost, and mechanical durability corroborate the potential of the floatable microbial device toward practical and sustainable solar energy conversion.

1. Introduction

Solar energy harvesting technologies[1–3] underpin the production of renewable energy sources[4,5] and the mitigation of carbon emissions.[6,7] Solar fuel synthesis using microbial systems,[8–10] in particular, is a vital emerging approach to environmentally sustainable solar energy conversion[11–13] due to its high selectivity,[14] feasibility,[15] and durability.[16,17] Efficient lab-scale microbial fuel production,[18–20] including microbial solar hydrogen (H_2) production,[21,22] has been achieved by recent research efforts such as advanced genetic engineering[23–25] and incorporation of semiconductor biohybrids.[26,27] However, the practical use of conventional microbial fuel production systems has been impeded, primarily by system-level design challenges such as ineffective supply of reactants and capture of

W. H. Lee, H. Park, G. D. Cha, B.-H. Lee, C. W. Lee, M. S. Bootharaju, S.-H. Sunwoo, J. Ryu, T. Hyeon, D.-H. Kim
Center for Nanoparticle Research
Institute for Basic Science (IBS)
Seoul 08826, Republic of Korea
E-mail: thyeon@snu.ac.kr; dkim98@snu.ac.kr

W. H. Lee, H. Park, G. D. Cha, B.-H. Lee, J. Lee, C. W. Lee, M. S. Bootharaju, S.-H. Sunwoo, J. Ryu, C. Lee, K. H. Ahn, T. Hyeon, D.-H. Kim
School of Chemical and Biological Engineering
and Institute of Chemical Processes
Seoul National University
Seoul 08826, Republic of Korea

C.-K. Yoon, G.-H. Park, T.-W. Nam, Y.-J. Seok
School of Biological Sciences and Institute of Microbiology
Seoul National University
Seoul 08826, Republic of Korea
E-mail: yjseok@snu.ac.kr

The ORCID identification number(s) for the author(s) of this article can be found under https://doi.org/10.1002/adma.202306092

DOI: 10.1002/adma.202306092

C.-K. Yoon
Research Institute of Basic Science
Seoul National University
Seoul 08826, Republic of Korea

J. H. Jeong
Department of Chemical Engineering
Stanford University
Stanford, CA 94305, USA

Y.-J. Cho
Department of Molecular Bioscience
College of Biomedical Science
Kangwon National University
Chuncheon, Gangwon 24341, Republic of Korea

Y.-J. Cho
Multidimensional Genomics Research Center
Kangwon National University
Chuncheon, Gangwon 24341, Republic of Korea

T.-W. Nam
MightyBugs, Inc.
Busan 46918, Republic of Korea

D.-H. Kim
Department of Materials Science and Engineering
Seoul National University
Seoul 08826, Republic of Korea

products[28,29] as well as by the requirement of electrodes[30,31] and scale-up issues.

For large-scale microbial solar fuel production, appropriate reactor or platform designs[32,33] of the photosynthetic systems[34,35] are highly important. The current designs are predominantly limited to the fed-batch-type (Figure S1a, Supporting Information) or flat-plate-type photoreactors[18,36] (Figure S1b, Supporting Information), which have general drawbacks with regard to the efficiency and performance of microbial photosynthesis. Both types commonly require massive agitation and forced convection (Figure S1a,b(i), Supporting Information) for the continuous supply of reactants and capture of products because of the sluggish gas diffusion in aqueous reaction media[37,38] (Figure S1a(ii), Supporting Information) and through closely-assembled microorganisms (Figure S1b(ii), Supporting Information), leading to high energy cost and poor system durability. Besides, scattering and absorption of light by reaction media tend to attenuate light intensity at microbial active sites, contributing to their low photosynthetic performance (Figure S1a,b(iii), Supporting Information). Furthermore, the flat-plate-biofilm photoreactors often suffer from poor immobilization of microorganisms on the substrate (Figure S1b(iv), Supporting Information), thereby limiting their long-term stability. As such, for efficient and scalable microbial photosynthesis, the design of prospective microbial reaction systems should consider facile mass transport of reactants and products, address the limitations of light attenuation within reaction media, and provide chemical and mechanical durability.

We herein present a novel design of the microbial photoreactor system that can circumvent the aforementioned challenges and thus enable efficient, scalable, and environmentally benign solar H_2 production using microbial metabolism. The most efficient H_2 production pathway of *Rhodopseudomonas parapalustris* (*R. parapalustris*) as a novel alternative to conventional nitrogen (N_2)-fixing microbes is firstly characterized in this work. Specifically, inspired by the water lily that lives in ponds but whose leaves exchange gases and absorb light efficiently by floating on water, we report an N_2-fixing floatable microbial device that harnesses unique environments at the gas-liquid interface to achieve facile supply of gaseous reactants, efficient capture of gaseous products, and effective light absorption. Encapsulation of the N_2-fixing microbes inside alginate hydrogel, supported by a deliberately engineered elastomer-hydrogel hybrid,[39] allows for reliable and robust immobilization of the microbes, facile supply of aqueous reactants through the porous hydrogel structure,[40] and desirable buoyancy of the entire system. The highly efficient N_2 fixation which brings a stark contrast in H_2 generation between floatable and sunken microbial devices as well as material durability, scalability, and economically feasible fabrication process of the device, illustrates its potential as a promising photosynthetic platform for economically feasible green energy conversion (Table S1, Supporting Information).

2. Results and Discussion

2.1. Overview of the Floatable Microbial Device

The floatable microbial device (**Figure 1**) incorporates *R. parapalustris* JA310 (Figure 1a), which can produce H_2 via the N_2 fixation mechanism as first reported in this work (more details in the next section). The detailed mechanism of N_2 fixation and H_2 production by *R. parapalustris* is illustrated in Figure 1b. Absorption of light energy facilitates cyclic electron transport between cytochrome b/c1 and cytochrome c in the light-harvesting system.[41,42] A proton gradient induced by the cyclic electron transport drives ATP synthesis[41–43] and the reduction of NAD^+ to NADH is driven by NADH dehydrogenase (NDH)-mediated reverse electron flow from ubiquinol (QH_2) using proton motive force (PMF) (Figure 1b).[44]

Organic substrates in the reaction medium serve as carbon sources and electron donors, reducing NAD^+ to NADH through glycolysis and the TCA cycle. Electrons stored in NADH are used to reduce three types of ferredoxins by Fix complex, and the reduced ferredoxin is also generated in the quinone pool during the photosynthetic process.[42,43] N_2 fixation involves the catalytic activity of nitrogenases and results in the simultaneous production of H_2 and ammonia.[45] However, the nitrogenase activity is switched off in the presence of external ammonia (orange box in Figure 1b).[46]

The floatable microbial device is designed to have a unique bilayer structure (Figure 1c) to mimic the floating leaves of water lilies (Figure 1d). As chloroplasts are mainly located in the upper epidermis of a leaf, the top layer of the device encompasses an alginate hydrogel biocomposite[47,48] containing *R. parapalustris*. While, the bottom supporting layer comprises macroporous hydrophilic polyurethane (HPU) and poly(propylene glycol) (PPG) polymers, inspired by the aerenchyma of water lily, to afford the desirable floatability of the entire system. The floatability of the device (**Figure 2**a,b) makes the microbial layer reside at phase boundaries, enabling a facile supply of gaseous reactants (e.g., N_2) (Figure 1c(i)) and instantaneous gas-phase diffusion of generated H_2 (Figure 1c(ii)). Such interphasic configurations of the device are beneficial not only for the mass transfer of gases improved by much higher gas diffusion rates in the air (Figure 1e) but also for efficient light delivery to microbes with minute attenuation of the light intensity at the microbial active sites (Figure 1c(iii) and Figure 2c). In addition, the high hydrophilicity and porosity of the microbial device facilitate the supply of water and aqueous reactants (e.g., carbon substrates) to microorganisms (Figure 1c(iv) and Figure 2d,e). Importantly, the supporting layer of the device also consists of a highly durable elastomer-hydrogel hybrid (HPU-PPG), which provides long-term mechanical stability[49–51] (Figure 1c(v) and Figure 2f-h).

Schematics and photographs that illustrate the fabrication process of the microbial device are shown in Figure 2i. First, HPU (orange chain)-PPG (blue chain)-sodium chloride (NaCl; gray circle) gel is synthesized (Figure 2i(i)). Then, the porous supporting layer is formed by solvent evaporation followed by the dissolution of NaCl granules in water (Figure 2i(ii)). Finally, the alginate hydrogel biocomposite (pink layer) including *R. parapalustris* (red oval) is integrated with the supporting layer through calcium chloride ($CaCl_2$) cross-linking process (Figure 2i(iii)).

2.2. Characterization of *R. Parapalustris*

At the outset of this study, we aimed to identify a desirable microbial system for efficient solar H_2 production. Among other species of photosynthetic *Rhodopseudomonas* bacteria,

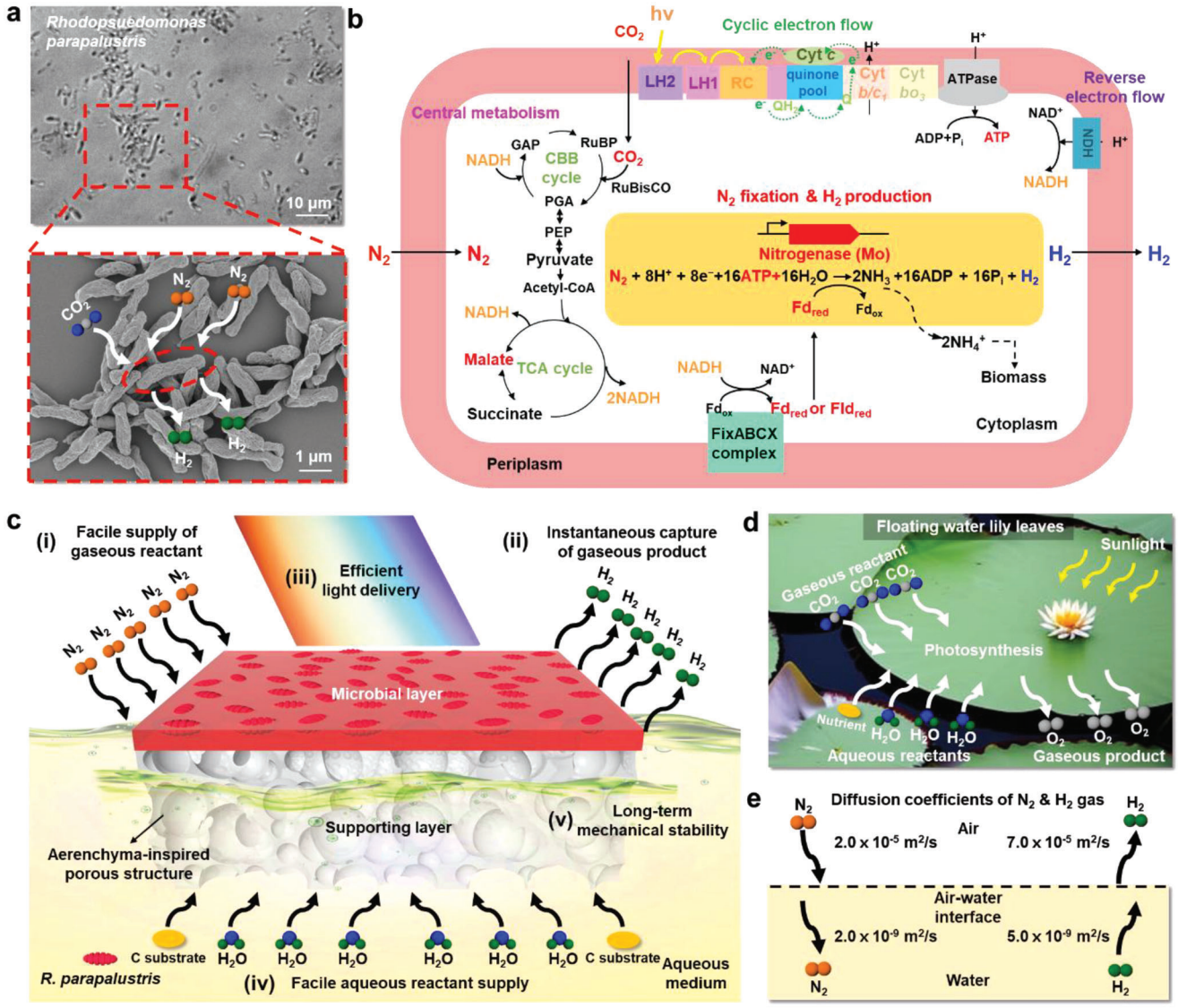

Figure 1. Overview of the floatable microbial device. a) Optical image (top) and scanning electron microscopy (SEM) image (bottom) of *Rhodopseudomonas parapalustris*, which generates H_2 via N_2 fixation. b) Schematic illustration showing the central metabolic pathway, photosynthetic electron transfer, reverse electron flow, and nitrogen fixation mechanism of *R. parapalustris* JA310. NDH, NADH dehydrogenase encoded by the genes in the *nuo* operon; Fd, ferredoxin encoded by *fer1* and *ferN*; Fld, flavodoxin encoded by *fldA*. c) Schematic illustration for the floatable microbial device and a brief description of its strengths in highly efficient N_2 fixation and H_2 production: i) facile supply of gaseous reactant, ii) instantaneous separation and capture of a gaseous product, iii) efficient light delivery, iv) facile supply of aqueous reactants, and v) long-term mechanical stability. d) Schematic illustration of the leaves of water lilies floating on water. Floatability facilitates efficient photosynthesis by facile transfer of gaseous reactant and aqueous reactants and smooth delivery of sunlight. e) Diffusion coefficients of N_2 and H_2 gas in air and water.

Rhodopseudomonas palustris (*R. palustris*) CGA009 is known for its versatility to acquire metabolic carbon from various natural organic compounds or by carbon dioxide (CO_2) fixation, undergo photoheterotrophic, photoautotrophic, chemoheterotrophic, and chemoautotrophic growth in different environments, and produce H_2 via N_2 fixation.[42] Unlike *R. palustris*, however, little is known about H_2 production and N_2 fixing behaviors of other *Rhodopseudomonas* spp, critically limiting their range of applications.[42]

As a novel alternative to *R. palustris*, we newly characterized *R. parapalustris* JA310 and examined its photosynthetic behaviors (**Figure 3**). We found that under photoheterotrophic conditions, *R. parapalustris* exhibits a growth rate (generation time: 8.81 h; Figure S2a, Supporting Information) comparable to the reported growth rate of *R. palustris* (generation time: 8.4 ± 0.6 h).[52] To assess whether *R. parapalustris* possesses physiological advantages over *R. palustris* (Figure 3a), we conducted genome sequencing of *R. parapalustris*. Using the Illumina platform, we revealed that *R. parapalustris* share 84% of the total 4657 orthologous gene clusters with *R. palustris*, including all of the genes responsible for N_2 fixation and H_2 production (Figure 3b and Table S2, Supporting Information). Comparative genomic

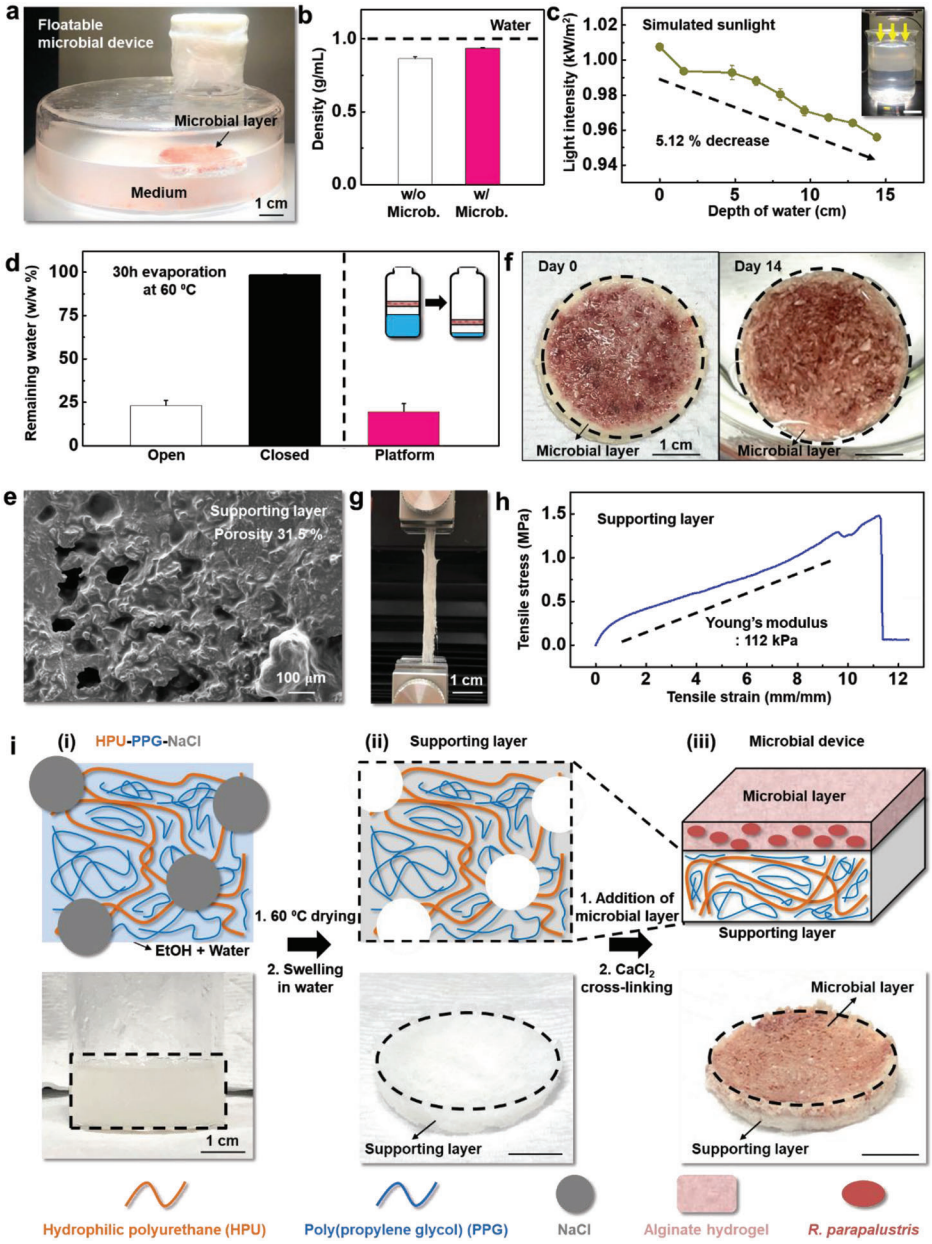

Figure 2. Characterization and fabrication process of the floatable microbial device. a) Optical image of a device floating on the media solution. b) Density of the microbial device without (left) and with (right) the microbial layer. The addition of a microbial layer induced a slight increase in density, implying a slight decrease in floatability, but the microbial device still exhibits floatability in water. c) Attenuation of light intensity as a function of the depth below the surface. Light intensity decreases in water due to scattering and absorption. The inset shows a photograph of a beaker filled with water (15 cm depth) and placed on the light intensity measurement apparatus (scale bar: 10 cm). d) Percentage of water remaining after 30 hours of evaporation at 60 ^{0}C in the oven (blue color in the top right inset) through the device (pale red line in the inset) for the open and closed systems. Control groups correspond to the open or closed systems without the device. e) SEM image of the HPU-PPG elastomer-hydrogel hybrid. g) Optical image of the stretched hydrogel. h) Tensile test of the HPU-PPG hydrogel. f) Optical images of the microbial device before (left) and after (right) swelling in water for 14 days. i) Schematic illustrations (top) and optical images (bottom) of the fabrication process of the device. i) HPU-PPG-NaCl gel is formed. ii) A supporting layer is formed through drying and swelling. iii) A microbial layer embedding *R. parapalustris* is integrated on the supporting layer by $CaCl_2$ cross-linking which facilitates the gelation of the alginate hydrogel biocomposite.

analysis of *R. palustris* CGA009 and *R. parapalustris* JA310 revealed that a complete cytochrome *bd*-1 gene cluster is conserved in both strains (Figure 3a). Interestingly, however, while *R. palustris* lacks CyoABCD components, *R. parapalustris* possesses a complete cytochrome bo_3 complex (CyoABCDE) (Figure 3a). Because the cytochrome bo_3 complex pumps protons more efficiently than the cytochrome *bd*-1 complex ($H^+/2e^-$ stoichiometry: 4 to 2),[53] *R. parapalustris* can generate a greater PMF than *R. palustris*. This increased PMF can facilitate *R. parapalustris* to produce more ATP and NADH (Figures 1b and 3a).

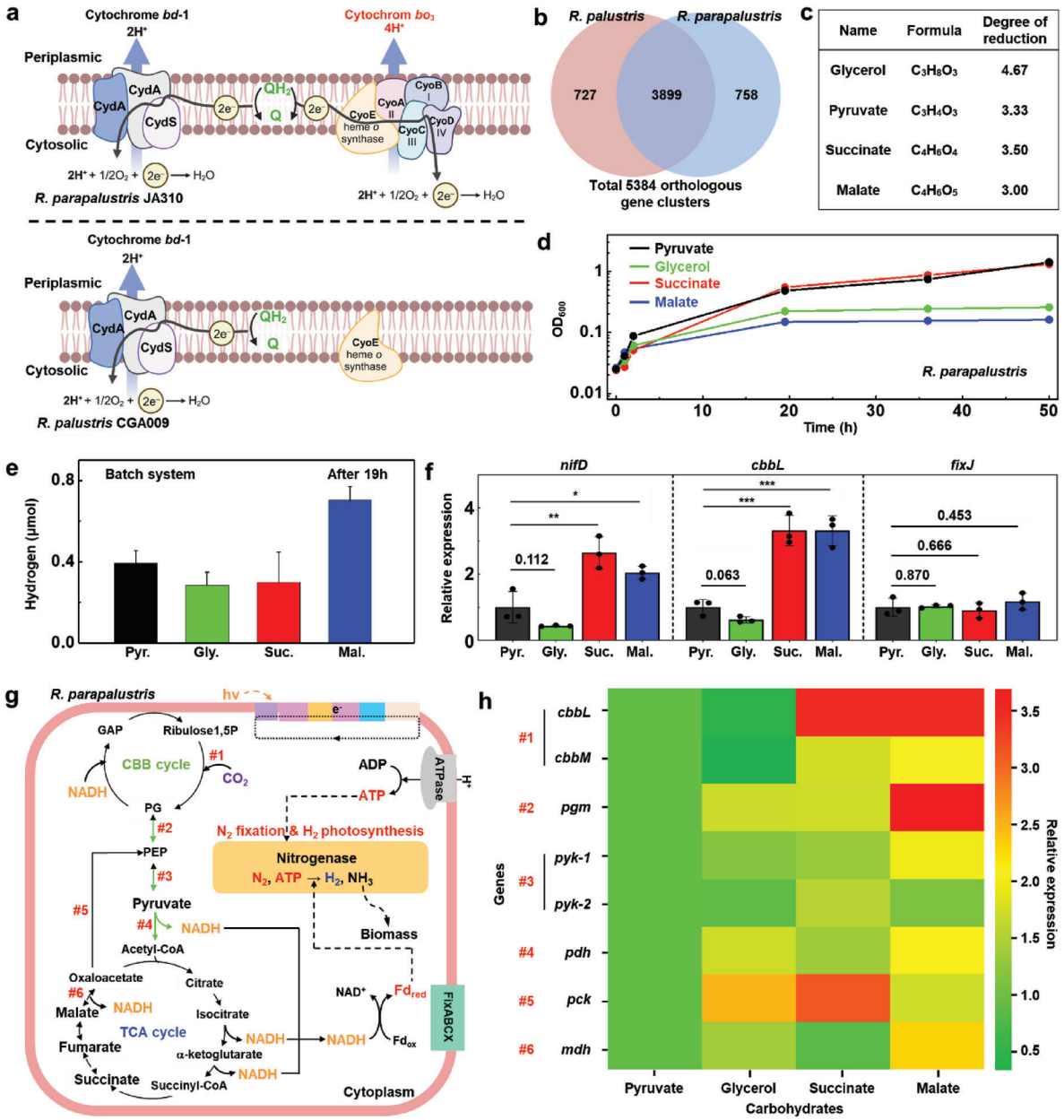

Figure 3. Characterization of *R. parapalustris*. a) Schematic illustration of the cytochrome *bd*-1 and bo_3 components in *R. parapalustris* JA310 and *R. palustris* CGA009. b) Venn diagram represents the result of comparative genomic analysis between *R. palustris* CGA009 and *R. parapalustris* JA310. The numbers in the areas indicate the number of orthologous gene clusters. *R. parapalustris* has a total of 4657 ortholog gene clusters, of which 3899 are shared with *R. palustris*. c) Formal degree of reduction of carbon substrates. d) Comparison of the growth of *R. parapalustris* JA310 strain in IFO802 medium supplemented with the indicated carbon substrates. e) H_2 generation yield from *R. parapalustris* grown on the indicated carbon substrate. f) Relative transcript levels of *nifD*, *cbbL*, and *fixJ* in *R. parapalustris* grown on indicated carbon substrates. The transcriptional level of *fixJ* was used as a negative control. Transcript levels are presented as a ratio relative to the reference, *rpoD* (***$p < 0.005$, **$p < 0.01$, *$p < 0.05$). g) Schematic illustration of the central metabolic fluxes in *R. parapalustris* strains during phototrophic growth. Metabolic pathways involved in the production of H_2 are noted with red numbers. h) Differential expression analysis of genes encoding the enzymes catalyzing the metabolic reactions in *R. parapalustris* (as shown in f)) grown on various carbon substrates. The mRNA levels are shown as a ratio relative to that of the cell grown on pyruvate. The mean values and standard deviations in e) and f) are obtained from three independent measurements.

Furthermore, it is known that *R. parapalustris* possesses a cell size aproximately 1.8 times larger than that of *R. palustris*.[54] Therefore, incorporating *R. parapalustris* into the hydrogel offers the advantage of reducing the likelihood of cell leakage and requiring fewer cells to occupy a given space. In addition, since the metabolism of the bacterial cell linearly scales with overall cell size,[55] *R. parapalustris* may exhibit a higher metabolic rate than *R. palustris*.

Along with the identified genetic potency, *R. parapalustris* exhibited photoheterotrophic growth on various carbon substrates,

such as pyruvate, glycerol, succinate, and malate, which serve as metabolic carbon sources and/or electron donors (Figure 3c,d). While the growth of *R. parapalustris* on malate was found to be slower than the growth on other carbon substrates (e.g., pyruvate and succinate), probably due to a lower reducing power of malate with its higher oxidation state (Figure 3c),[56] the malate-grown cells of *R. parapalustris* showed a two-fold increase in H_2 production rate compared to the cells grown on other carbon substrates, which implies that electrons are shifted away from CO_2 fixation or biomass formation to H_2 production as seen in *R. palustris* (Figure 3e).[57] We found that the expression of NifD, which encodes the dinitrogenase component of Mo-nitrogenase,[58] was significantly increased in malate- or succinate-grown cells than in the cells grown on glycerol or pyruvate (Figure 3f). These results suggest that the H_2 production coupled with N_2 fixation is actively occurring in malate- or succinate-grown *R. parapalustris* (see below sections for more evidence), similar to the fumarate-grown *R. palustris* strain that constitutively produces H_2 via nitrogenase.[57]

We also examined the relationship between the photosynthetic production of H_2 and the operation of the Calvin-Benson-Bassam (CBB) cycle within the malate-grown *R. parapalustris*. For various photosynthetic bacteria, nitrogenase-based H_2 production and operation of CO_2 fixation by ribulose 1,5-bisphosphate carboxylate (RuBisCO) are known to be mutually exclusive. This is because the two processes compete with each other for electrons from reduced electron carriers (such as NADH or ferredoxins).[52] In contrast to the trend, however, the malate-grown cells of *R. parapalustris* showed a simultaneous increase in expression of both genes encoding RuBisCO (e.g., CbbL and CbbM) and NifD (Figure 3f,h). To rationalize this odd behavior, we compared expression levels of enzymes catalyzing the reaction in the metabolic pathway between the CBB cycle and the TCA cycle (Figure 3g). As a result, we found that the expression of enzymes responsible for the pathway from malate to acetyl-CoA was significantly increased in the malate-grown cells (Figure 3h). The enhanced pathway may contribute to the increase in electron carrier reduction flux (e.g., NADH), which can compensate for the augmented oxidation flux from simultaneously promoted CO_2 fixation and H_2 production via N_2 fixation.[57] Although both succinate- and malate-grown *R. parapalustris* exhibit elevated expression of the nitrogenase gene (Figure 3f), malate-grown cells exhibit higher H_2 production than succinate-grown cells (Figure 3e). In *R. palustris* expressing an increased level of nitrogenase, cells grown on fumarate/malate exhibit higher hydrogen production compared to succinate-grown cells because electrons are shifted away from CO_2 fixation towards H_2 production.[57] Therefore, we assumed that malate-grown *R. parapalustris* exhibit higher H_2 production compared to that of succinate-grown *R. parapalustris*.

2.3. Solar H_2 Production by the Floatable Microbial Device

With the characterized microbe in hand, we next assembled it into a floatable device (Figure S3a, Supporting Information) and examined its H_2-generating performance under simulated sunlight (air mass (AM) 1.5G condition; **Figure 4**a). The floatable device generates H_2 at a rate of 104 mmol h^{-1} m^{-2}, even without forced convection of medium (Figure 4b,c and Figure S3b-d, Supporting Information). Importantly, we observed a rapid decrease (Figure 4d(i)) and saturation (Figure 4d(ii)) of ammonium ion (NH_4^+) in the aqueous medium during H_2 production, which is a clear indication of the operation of N_2 fixation via nitrogenase in *R. parapalustris*[46] (Figure 4b,c). Equipped with the mechanical durability of the constituent elastomer-hydrogel hybrid, the floatable system also shows stable N_2 conversion (Figure S3f, Supporting Information) and H_2 generation for three cycles (Figure 4e and Figure S3g, Supporting Information). In addition, compared with the fabrication costs of common H_2-generating photocatalysts such as Pt/TiO_2 (6500–9700 \$ kg^{-1}) nanoparticles, estimated by CatCost, the fabrication cost of *R. parapalustris*, N_2-fixing biocatalyst, is estimated to be relatively lower,[39] which suggests its potential use in the commercially feasible microbial device.

To verify the essential benefits of our floatable design, we compared the H_2 production rate of the floatable device to that of the sunken device placed at a depth of 2 cm from the water surface by imposing weight but prepared under otherwise identical conditions (Figure 4a). Indeed, the sunken device exhibits a 53 times lower rate of H_2 production (1.96 mmol h^{-1} m^{-2}) and correspondingly sluggish N_2 conversion (Figure S3e, Supporting Information) compared to those of the floatable device. Notably, in the case of previously reported photocatalytic nanocomposites, the floatable nanocomposite exhibited only a two-fold increase in the H_2 evolution rate, compared with that of the sunken nanocomposite.[39] We assume that the stark contrast between floatable and sunken microbial devices (a 53-fold increase) originates from the improved mass transport of not only product (H_2) but also reactant (N_2) through the gas phase since the floatable device is placed at the air-water interface (Figure 1c–e), which does not apply to the sunken device.

Numerical simulations for the lab-scale devices (3 cm-scale) evince the postulated scenarios (Figure S4a, Supporting Information). When we simulated the concentration distributions of N_2 and H_2 at different time points (1, 5, 20, 100, 200, 400, and 600 min) for both floatable and sunken devices (Figure 4f–i and Figure S4b-e, Supporting Information), the H_2 concentration in the air increases remarkably for the floatable device, whereas a negligible change in the H_2 concentration in the air is observed for the sunken device. Besides, a significant decrease in the H_2 concentration inside the medium is observed for the sunken device by the increases in the depth from the water surface (Figure S4e, Supporting Information). The additional simulation predicts an even greater difference in the H_2 production rates between the floatable device and the sunken device in their enhanced model sizes (Figure S5, Supporting Information), thereby manifesting the scalable benefits of the floatable device design.

2.4. Scale-Up of the Floatable Microbial Device

To demonstrate scalable H_2 production, the device size is increased from 9.62 to 144 cm^2 (**Figure 5**). The illustration and optical images of the H_2 generation system, incorporating the 12 × 12 cm^2 microbial device (Figure S6a, Supporting Information), are presented in Figure 5a,b, respectively. The scaled-up reactor is comprised of a steel cell (dimension: 23 × 23 × 7 cm^3) with an inlet and outlet for the aqueous medium and four junctions to

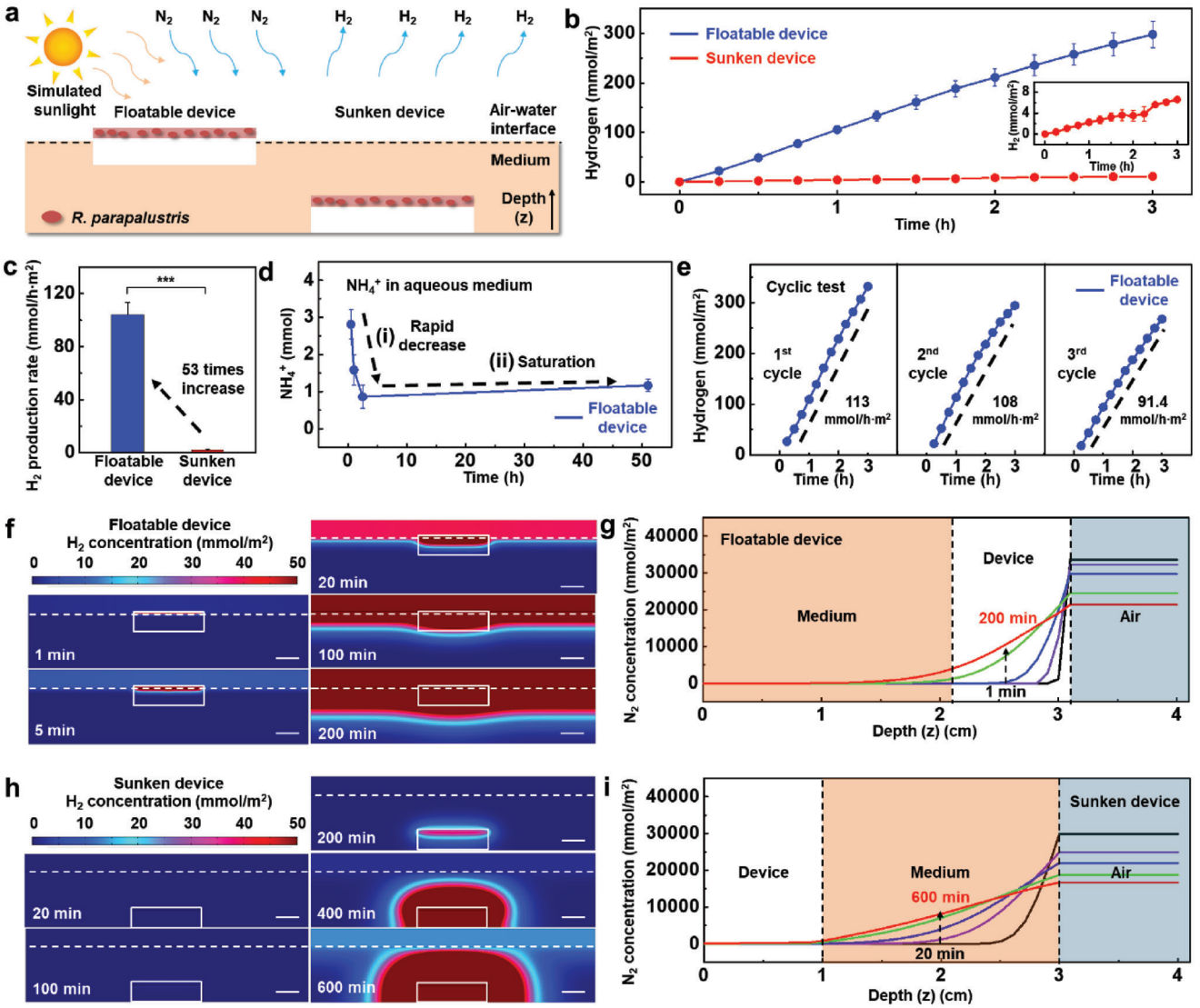

Figure 4. Solar H_2 production by the floatable microbial device. a) Schematic illustration of the floatable and sunken devices during microbial N_2 fixation and H_2 production. b) Time course of H_2 generation by the floatable (blue) and sunken (red) devices under simulated sunlight. The inset shows a magnified view of the H_2 generation by the sunken device. c) H_2 production rate of the floatable (blue, 104 mmol h^{-1} m^{-2}) and sunken (red, 1.96 mmol h^{-1} m^{-2}) devices (***$p < 0.001$ by independent samples t-test). d) Time course of NH_4^+ in an aqueous medium while simulated sunlight is irradiated on the floatable device, showing i) a rapid decrease followed by ii) saturation. e) Time course of H_2 generation by the floatable device during the cyclic test. f) H_2 concentration distribution (scale bar: 1 cm) and g) N_2 concentration as a function of the depth (z) of the aqueous medium for the floatable device at various time points: 1 min (black), 5 min (purple), 20 min (blue), 100 min (green), and 200 min (red). h) H_2 concentration distribution (scale bar: 1 cm) and i) N_2 concentration as a function of the depth (z) of the aqueous medium for the sunken device at various time points: 20 min (black), 100 min (purple), 200 min (blue), 400 min (green), and 600 min (red), estimated by the simulation.

connect with polyurethane tubes and a quartz window (dimension: 15 × 15 × 3 cm^3) as shown in Figure 5a–c.

Equipped with this setup, the enlarged device exhibits an H_2 production rate of 1.52 L h^{-1} m^{-2} (Figure 5d) and an N_2 conversion rate of 1.83% (Figure S6b, Supporting Information) under simulated sunlight of one-sun intensity (AM 1.5G; Figure 5c). We note that the measured H_2 generation rate, corresponding to 0.489 mmol h^{-1} (Figure S6c, Supporting Information), is higher than the largest microbial H_2 production rates previously reported thus far (Table S1, Supporting Information). Computational simulations on the microbial N_2 fixation and H_2 generation with 1 m^2-scale device (Figure 5e-h and Figure S7, Supporting Information) corroborate that the unique advantages of our floatable design remain intact regardless of its size, thereby presenting a possibility for the large-scale N_2 fixation and H_2 production from the proposed design.

3. Conclusion

In conclusion, we report a floatable microbial device, which shows excellent and scalable performance for H_2 production via N_2 fixation. We demonstrate the essential benefits of the floatable

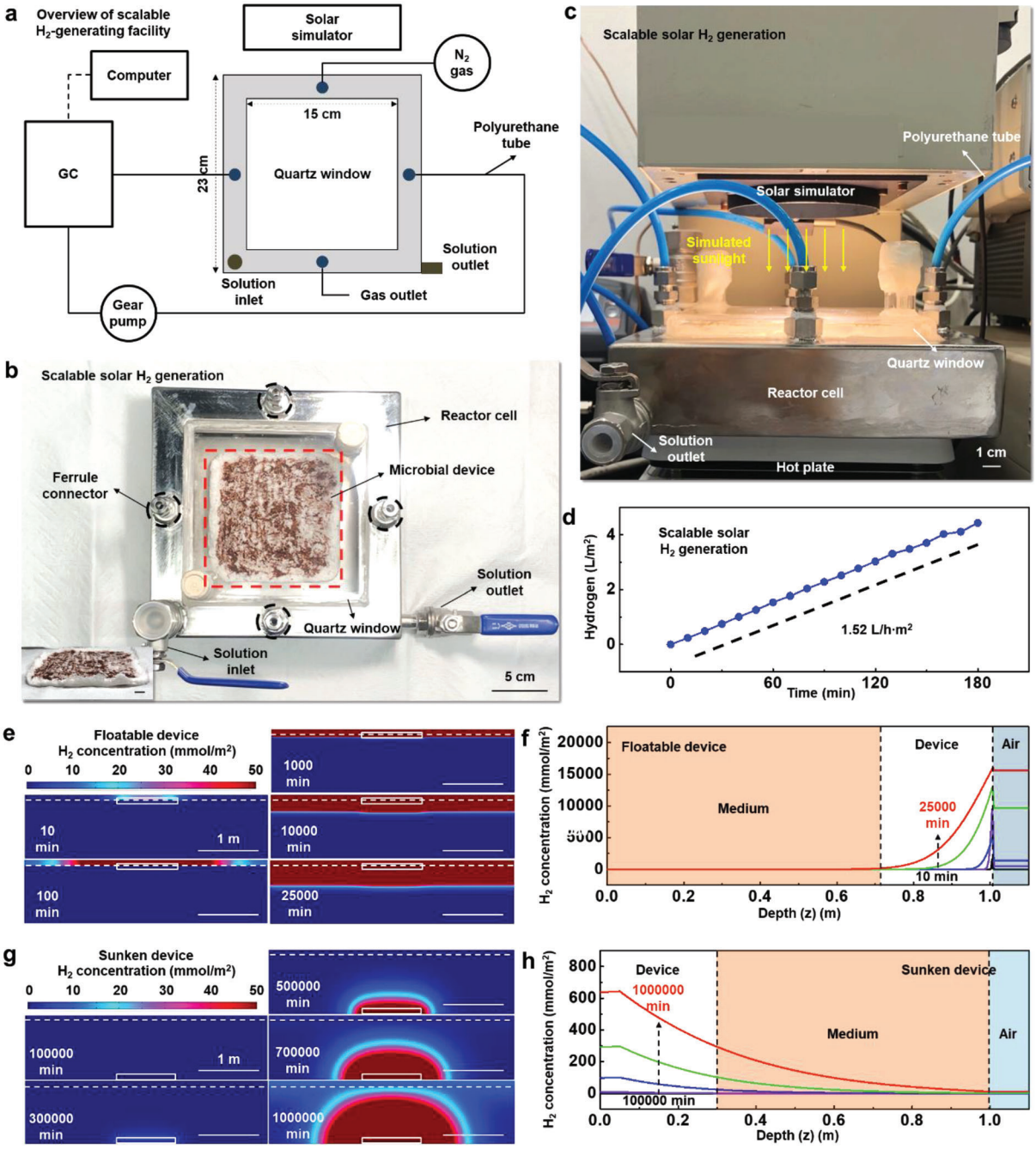

Figure 5. Scale-up of the floatable microbial device. a) Schematic diagram of the design of a scalable H_2 generation device. b) Optical image of the scaled-up microbial device, assembled in the reactor cell. The inset shows a side view of the device with a length of 12 cm and a width of 12 cm. c) Optical image of the reactor cell for the scale-up of solar H_2 production under the solar simulator (AM 1.5 G illumination). d) Time course of H_2 generation by the scaled-up floatable device. e) H_2 concentration distributions and f) H_2 concentration as a function of the depth (z) of the aqueous medium for the floatable device and g) H_2 concentration distributions and h) H_2 concentration as a function of the depth (z) of the aqueous medium for the sunken device at various time points (e.g., 10, 100, 1000, 10 000, 25 000, 100 000, 300 000, 500 000, 700 000, and 1 000 000 min), estimated by the 1 m^2-scale simulation.

design with its superior performance over the control sunken-type microbial device, as shown by both experiments and theories. We also showcased the scalability of our designs with the enlarged setup, which is further corroborated by the 1 m^2-scale simulation. The high efficiency of H_2 generation, material durability, scalability, and economically feasible fabrication process of the microbial device, in the aggregate, support its great potential as a commercially viable photosynthetic platform for large-scale green energy conversion. Future investigations on diverse electron donors for efficient electron transfer to hydrogen and

additional examination of the molecular-level mechanism of the photo-oxidative stress response in *R. parapalustris* are needed in the future, which will be helpful to enhance the utility of the microbial device.[59,60]

4. Experimental Section

Materials: Poly(propylene glycol) (PPG), sodium chloride (NaCl), and ethanol (EtOH) were purchased from Samchun Chemicals. Hydrophilic polyurethane (HPU) was purchased from Aekyung Chemical. Peptone, yeast extract, and magnesium sulfate heptahydrate ($MgSO_4 \cdot 7H_2O$) were purchased from Thermo Fisher Scientific.

Bacterial Strains and Culture Conditions: The *R. parapalustris* strain JA310 used in this study was purchased from Korean Collection for Type Culture (Jeongeup, Korea) and was cultured under photosynthetic conditions (5% CO_2, 5% H_2, and 90% N_2 in front of an incandescent light source with an intensity of 18.96 W m^{-2}) at 32°C in IFO802 medium supplemented with the indicated filter-sterilized carbon sources (final concentration: 0.3% w/v).[61] The IFO802 medium contained (per 100 mL) 1 g of peptone, 0.2 g of yeast extract, and 0.1 g of $MgSO_4 \cdot 7H_2O$.

Fabrication of the Microbial Device: Three milliliters of HPU solution (HPU in water, 50 wt%) was prepared and EtOH was added to the solution to set the concentration of HPU as 10.5 wt%. After mixing, NaCl was added to the above solution with a concentration of 0.032 g mL^{-1}. After vigorous stirring of the solution, PPG was added to the solution with a volume ratio of 1:2 (PPG:HPU). A mixed sol–gel state was formed after adding PPG, and the gel phase was separated after 3 h. The gel was molded into a circular shape with a diameter of 3.5 cm. After molding, water and EtOH left in the gel phase were evaporated by drying at 60 °C for 24 h, and the gel phase was swollen with water to remove NaCl granules in the HPU-PPG elastomer–hydrogel hybrid. The obtained hydrogel was sterilized with 70% EtOH, irradiated under UV, and autoclaving with Classic Media autoclave (Prestige Medical, UK). *R. parapalustris* JA310 cells were grown in the IFO802 medium for 3 days until OD reaches 2.5. Cells (60 mL; 0.89 g wet weight) were centrifugated at 4000 × *g* for 10 min. The pellet was resuspended with 2 mL of 2% alginate solution resolved in autoclaved IFO802 medium supplemented with filtered 0.3% malate. The alginate–cell mixture was spread onto the hydrogel device followed by cross-linking with 10% $CaCl_2$ and washing with phosphate-buffered saline. Fabrication of the microbial device in a scalable size was started with 60 mL of HPU and it follows the same procedures as the above method except molding in a square shape with a length of 12 cm and a width of 12 cm.

Field Emission Scanning Electron Microscopy (FESEM): *R. parapalustris* cells (100 µL) cultured in the IFO802 medium were spread onto the IFO802 agar plate and incubated for 24 h under photosynthetic conditions. Ten individual colonies were picked and suspended in 500 µL of PBS. The microscopic sample was prepared as previously reported.[62] Scanning electron microscopy images were obtained using a field-emission scanning electron microscope (Sigma 55VP, Carl Zeiss, United Kingdom) using an acceleration voltage of 15 kV (NICEM, Seoul, Korea).

Bacterial Genome Sequencing and Analysis: The genomic DNA of *R. parapalustris* was extracted using the QIAamp DNA Mini Kit (Qiagen, Germantown, MD) and 100 ng of genomic DNA was processed for the next step. The sequencing library was constructed by using a TruSeq Nano DNA kit (Illumina, USA, #20015964) according to the manufacturer's instructions. Whole genome sequencing was performed by the NovaSeq platform (Illumina, USA) and generated 151 bp paired-end data, and a total of 3.36 Gb of data were obtained from 22282426 reads. Resulted raw data were cleaned and assembled using clc genomics workbench 21 (Qiagen, Germantown, MD). The total genome assembly size was 5.39 Mb in 83 contigs containing 5018 genes with 599.9× coverage. The annotation of the genome was performed at The NCBI Prokaryotic Genome Annotation Pipeline.[63] The genome sequence has been deposited in GenBank under the accession PRJNA841417. Ortholog clustering between *R. palustris* CGA009 and *R. parapalustris* JA310 was performed using panX.[64]

RNA Extraction and Quantitative Real-time Reverse Transcription-PCR (qRT-PCR): After fixing the cells (2 mL) with the same volume of 100% methanol for 1 h at −20 °C, total RNA was isolated using the TaKaRa MiniBEST Universal RNA Extraction Kit (Takara Bio, Inc., Otsu, Japan, #9767) following the manufacturer's instructions. Total RNA (2500 ng) from each sample was converted to cDNA using the RNA to cDNA EcoDry Premix (Random Hexamers) (Clontech Laboratories, Inc., Mountain View, CA, USA #639545). Twenty-fold diluted cDNA was subjected to real-time PCR amplification using FAST SYBR Green Master Mix (Thermo Fisher Scientific, Inc., Waltham, MA, USA, # 4385616) with specific primers (Table S3, Supporting Information) in a CFX96 Real-Time System (Bio-Rad, Hercules, CA, USA).[65] The transcript level of each metabolic gene is presented as a ratio relative to the reference, *rpoD*. For comparison of those values between cells grown on different carbon substrates, the mRNA levels are shown as relative values to that of the cells grown on pyruvate. An unpaired t-test was performed using Graphpad prism software.

Characterization of the Microbial Device: The floatability of the microbial device was measured by evaluating the equilibrium density. The microbial device was dropped into a solution of deionized water (density: 1 g mL^{-1}) and a pre-calculated amount of acetonitrile (density: 0.786 g mL^{-1}). The amount of acetonitrile added to the solution was controlled to adjust the density. The equilibrium density was determined as the density of the external solution when the device sinks into the solution. The mass transfer of water through the device was determined by measuring the amount of water evaporation through the device. The evaporated amount of water through the device was measured by measuring the weight difference of water covered by the device in a vial after storage for 30 h in the oven at 60 °C. The evaporated amount of water in an open state and closed state were also measured as positive control and negative control, respectively. The cross-section of the hydrogel was observed by a field emission scanning electron microscope (FESEM; Carl Zeiss) operated at 2.00 kV at the National Instrumentation Center for Environmental Management (NICEM) of Seoul National University. The porosity was calculated by the following equation: porosity $(\%) = (1 - \frac{W_{fd}}{W_{ww}}) \times 100$, in which W_{ww} and W_{fd} denote the mass of the fully swollen hydrogel and the hydrogel sample of which water in pores was eliminated, respectively. The tensile test was conducted to measure the elastic modulus of the HPU-PPG elastomer-hydrogel hybrid with a universal testing machine (UTM, 1 kN load-cell, Instron-5543) at a speed of 3.50 mm $^{-1}$s by following a modified version of ISO 527

H_2 Production Rate Measurements: The microbial H_2 production was conducted in a gas-sealed quartz cell reactor. The microbial device was floated on the IFO802 media solution supplemented with 0.3% malate. The sealed reactor was purged with nitrogen (N_2) gas for 20 min, and the device was irradiated with a solar simulator (ASTM E 927-05, Newport). The solar simulator emitted 100 mW cm^{-2} of simulated solar light (AM 1.5G) with square shape projection (8.5 × 8.5 cm^2) to the microbial device. The reaction temperature was set at 37 °C using a hot plate (MTOPS, HDS180). The hydrogen (H_2) generation was measured by using gas chromatography (iGC7200A, DS Science) with a thermal conductivity detector. The scalable microbial H_2 production was conducted in a gas-sealed steel cell reactor. The steel cell and quartz window were fixed with a silicone sealant after placing the microbial device and medium inside the reaction cell. A gear pump (Lead Fluid, CT3001F) was connected with the gas chromatography system and steel cell via polyurethane tubes in the head-space of the reactor cell for circulation of the gaseous environment. The sealed steel cell reactor was purged with nitrogen gas for 45 min, and the scaled-up device was irradiated by the solar simulator at the same temperature. The hydrogen generated by the device was measured by gas chromatography. The N_2 conversion rate was calculated by the metabolic mechanism of nitrogenase in *R. parapalustris* (Figure 1b). Ammonium ion (NH_4^+) was detected using an ion chromatograph (Dionex Aquion IC System., Thermo Fisher Scientific Inc, Waltham, USA) equipped with an SC-CERS 500 electrolytically regenerated suppressor and conductivity detector. Separation was achieved on an Ion Pac column (CS16, 5 × 250 mm) and a guard column (CG16, 5 × 50 mm) with an eluent of 30 mM methane sulfonic acid

flowing at a rate of 1.0 mL min^{-1}. The oven temperature was maintained at 40 °C and the current was set to 88 mA.

Numerical Simulation—Simulation domain: Figures S4a,S5a, and S7a (Supporting Information) illustrate the schematic diagram of lab-scale, scalable-size, and large-scale devices, respectively. A 2D simulation domain with the same width and height as in the experiment was considered. At first, N_2 existed only in the air region, with the initial concentration $[N_2]_0 = 0.0354$ M. As the simulation proceeded, N_2 diffused into both the device region and the water region. When N_2 touched the device region, the reaction of H_2 generation occurred. This reaction occurred only in the upper 0.1 cm-height region of the device, considering the thickness and location of the microbial layer in the device. The H_2 generated in the upper region of the device diffused into the device, water, and air region. The open boundary condition was applied, indicated by the dotted line.

Numerical Simulation—Governing Equations: The reaction of H_2 generation in the upper 0.1cm-height region of the device was considered. These two factors were included in the conservation equation as follows:

$$\frac{\partial c_i}{\partial t} = D_i \nabla^2 c_i + R_i \quad (1)$$

where c_i is the concentration of component i ($i = N_2$ or H_2), t is time, and D_i is the diffusion coefficient of component i. The diffusion coefficient of N_2 was set as 2×10^{-5} cm^2 s^{-1} in the device and water[37] and 0.2 cm^2 s^{-1} in air,[28] and the diffusion coefficient of H_2 as 5×10^{-5} cm^2 s^{-1} in the device and water,[38] and 0.7 cm^2 s^{-1} in air.[29] R_i indicates the reaction rate of component i, and it is assumed that the H_2 generation rate is equal to the N_2 consumption rate. Michaelis–Menten's model was chosen to express the H_2 generation rate, which was suitable for describing biochemical reactions. The expression is as follows:

$$R_{H_2} = \frac{k_r[N_2]}{K_M + [N_2]} \quad (2)$$

where k_r is the rate constant, and K_M is the Michaelis constant. To obtain k_r and K_M, the equation was fitted with the H_2 concentration-time graph in experimental results. First, in the floatable device, the initial concentration of N_2 was so large compared to K_M that K_M can be ignored in Equation 2. Thus, k_r can be obtained from the slope of the H_2 concentration-time graph. After that, K_M can be calculated from the results in the sunken device. Two constants in Equation 2 are as follows: $k_r = 1.92\times10^{-3}$ M s^{-1} and $K_M = 5.1\times10^{-4}$ M.

The commercial software COMSOL Multiphysics 5.4 (COMSOL Inc.) was used to discretize the simulation domain and to numerically solve the conservation equation. The simulation domain was discretized into ≈9000 elements, and the conservation equation was solved based on the finite element method solver in COMSOL. The numerical calculation was done in a workstation with two octa-core processors (Intel Xeon CPUs E5-2687 W 3.1 GHz) and 192 GB of memory.

Statistics: The experimental results of the H_2 production rate were compared and evaluated using the independent samples t-test.

Supporting Information

Supporting Information is available from the Wiley Online Library or from the author.

Acknowledgements

This research was supported by the Institute for Basic Science (IBS-R006-D1 and IBS-R006-A1), National Research Foundation (NRF) of Korea (NRF-2018R1A5A1025077 and NRF-2019R1A2C2004143 to C.-K.Y., G.-H.P., and Y.-J.S., and 2021R1A6A3A01086821 to C.-K.Y.).

Conflict of Interest

The authors declare no conflict of interest.

Author Contributions

W.H.L., C.-K.Y., H.S.P., and G.-H.P. contributed equally to this work. W.H.L., C.-K.Y., H.S.P., G.-H.P., T.H., Y.-J.S, and D.-H.K. conceived the ideas, designed the experiments, and wrote the manuscript. W.H.L., C.-K.Y., H.S.P., G.-H.P., G.D.C., B.-H.L., J.L., C.W.L., M.S.B., S.-H.S., J.R., C.L., Y.-J.C., T.-W.N., T.H., Y.-J.S., and D.-H.K. performed experiments and data analysis. J.H.J. and K.H.A. performed computer simulations.

Data Availability Statement

The data that support the findings of this study are available from the corresponding author upon reasonable request.

Keywords

applied microbiology, biocatalysis, energy harvesting device, hydrogel biocomposite, nitrogen fixation, solar energy conversion, sustainable hydrogen energy

Received: June 23, 2023
Revised: September 20, 2023
Published online: October 26, 2023

[1] X. Lang, X. Chen, J. Zhao, *Chem. Soc. Rev.* **2014**, *43*, 473.
[2] C. Gao, T. Wei, Y. Zhang, X. Song, Y. Huan, H. Liu, M. Zhao, J. Yu, X. Chen, *Adv. Mater.* **2019**, *31*, 1806596.
[3] Q. Wang, T. Hisatomi, Q. Jia, H. Tokudome, M. Zhong, C. Wang, Z. Pan, T. Takata, M. Nakabayashi, N. Shibata, Y. Li, I. D. Sharp, A. Kudo, T. Yamada, K. Domen, *Nat. Mater.* **2016**, *15*, 611.
[4] D. M. Schultz, T. P. Yoon, *Science* **2014**, *343*, 1239176.
[5] Y. Goto, T. Hisatomi, Q. Wang, T. Higashi, K. Ishikiriyama, T. Maeda, Y. Sakata, S. Okunaka, H. Tokudome, M. Katayama, S. Akiyama, H. Nishiyama, Y. Inoue, T. Takewaki, T. Setoyama, T. Minegishi, T. Takata, T. Yamada, K. Domen, *Joule* **2018**, *2*, 509.
[6] Y. Su, S. Cestellos-Blanco, J. M. Kim, Y.-X. Shen, Q. Kong, D. Lu, C. Liu, H. Zhang, Y. Cao, P. Yang, *Joule* **2020**, *4*, 800.
[7] R. G. Grim, J. R. Ferrell Iii, Z. Huang, L. Tao, M. G. Resch, *Joule* **2023**, *7*, 1684.
[8] H. Zhang, H. Liu, Z. Tian, D. Lu, Y. Yu, S. Cestellos-Blanco, K. K. Sakimoto, P. Yang, *Nat. Nanotechnol.* **2018**, *13*, 900.
[9] S. Cestellos-Blanco, H. Zhang, J. M. Kim, Y.-X. Shen, P. Yang, *Nat. Catal.* **2020**, *3*, 245.
[10] C. Trncik, F. Detemple, O. Einsle, *Nat. Catal.* **2023**, *6*, 415.
[11] S. Kruse, T. Goris, M. Westermann, L. Adrian, G. Diekert, *Nat. Commun.* **2018**, *9*, 4872.
[12] A. Wang, J. Zhang, L. Razzari, H. Liu, X. Yu, X. Jin, X. Chen, J. Zhang, Z. Zhao, M. Gao, *ACS Nano* **2020**, *14*, 13876.
[13] B. T. X. Hu, Z. ZHan, J. Zhang, I. Hussain, *Nat. Commun.* **2021**, *12*, 1.
[14] X. Fang, S. Kalathil, E. Reisner, *Chem. Soc. Rev.* **2020**, *49*, 4926.
[15] N. Kornienko, J. Z. Zhang, K. K. Sakimoto, P. Yang, E. Reisner, *Nat. Nanotechnol.* **2018**, *13*, 890.
[16] F. M. Schwarz, J. Moon, F. Oswald, V. Müller, *Joule* **2022**, *6*, 1304.
[17] D. Wu, W. Zhang, B. Fu, Z. Zhang, *Joule* **2022**, *6*, 2293.
[18] Q. Wang, S. Kalathil, C. Pornrungroj, C. D. Sahm, E. Reisner, *Nat. Catal.* **2022**, *5*, 633.
[19] Y. Honda, H. Hagiwara, S. Ida, T. Ishihara, *Angew. Chemie – Int. Ed.* **2016**, *55*, 8045.
[20] M. A. Emmanuel, S. G. Bender, C. Bilodeau, J. M. Carceller, J. S. Dehovitz, H. Fu, Y. Liu, B. T. Nicholls, Y. Ouyang, C. G. Page, T. Qiao,

F. C. Raps, D. R. Sorigué, S.-Z. Sun, J. Turek-Herman, Y. Ye, A. Rivas-Souchet, J. Cao, T. K. Hyster, *Chem. Rev.* **2023**, *123*, 5459.
[21] T. Li, Q. Jiang, J. Huang, C. M. Aitchison, F. Huang, M. Yang, G. F. Dykes, H.-L. He, Q. Wang, R. S. Sprick, A. I. Cooper, L.-N. Liu, *Nat. Commun.* **2020**, *11*, 5448.
[22] H. Shen, Y.-Z. Wang, G. Liu, L. Li, R. Xia, B. Luo, J. Wang, D. Suo, W. Shi, Y.-C. Yong, *ACS Catal.* **2020**, *10*, 13290.
[23] S. Rumpel, J. F. Siebel, C. Farès, J. Duan, E. Reijerse, T. Happe, W. Lubitz, M. Winkler, *Energy Environ. Sci.* **2014**, *7*, 3296.
[24] A. Wegelius, N. Khanna, C. Esmieu, G. D. Barone, F. Pinto, P. Tamagnini, G. Berggren, P. Lindblad, *Energy Environ. Sci.* **2018**, *11*, 3163.
[25] C. Zhan, X. Li, G. Lan, E. E. K. Baidoo, Y. Yang, Y. Liu, Y. Sun, S. Wang, Y. Wang, G. Wang, J. Nielsen, J. D. Keasling, Y. Chen, Z. Bai, *Nat. Catal.* **2023**, *6*, 435.
[26] B. Wang, C. Zeng, K. H. Chu, D. Wu, H. Y. Yip, L. Ye, P. K. Wong, *Adv. Energy Mater.* **2017**, *7*, 1.
[27] B. Luo, Y.-Z. Wang, D. Li, H. Shen, L.-X. Xu, Z. Fang, Z. Xia, J. Ren, W. Shi, Y.-C. Yong, *Adv. Energy Mater.* **2021**, *11*, 2100256.
[28] C. S. Ellis, J. N. Holsen, *Ind. Eng. Chem. Fundam.* **1969**, *8*, 787.
[29] N. Matsunaga, M. Hori, A. Nagashima, *Heat Transf. Res.* **2002**, *31*, 182.
[30] A. J. Mccormick, P. Bombelli, D. J. Lea-Smith, R. W. Bradley, A. M. Scott, A. C. Fisher, A. G. Smith, C. J. Howe, *Energy Environ. Sci.* **2013**, *6*, 2682.
[31] H. Wang, F. Qian, G. Wang, Y. Jiao, Z. He, Y. Li, *ACS Nano* **2013**, *7*, 8728.
[32] L. Lu, N. Ren, X. Zhao, H. Wang, D. Wu, D. Xing, *Energy Environ. Sci.* **2011**, *4*, 1329.
[33] Z. Xu, S. Wang, C. Zhao, S. Li, X. Liu, L. Wang, M. Li, X. Huang, S. Mann, *Nat. Commun.* **2020**, *11*, 5985.
[34] G. Saper, D. Kallmann, F. Conzuelo, F. Zhao, T. N. Tóth, V. Liveanu, S. Meir, J. Szymanski, A. Aharoni, W. Schuhmann, A. Rothschild, G. Schuster, N. Adir, *Nat. Commun.* **2018**, *9*, 2168.
[35] A. Bandyopadhyay, J. Stöckel, H. Min, L. A. Sherman, H. B. Pakrasi, *Nat. Commun.* **2010**, *1*, 139.
[36] Y. Chen, *Energy Environ. Sci.* **2022**, *15*, 2843.
[37] S. P. Cadogan, G. C. Maitland, J. P. M. Trusler, *J. Chem. Eng. Data* **2014**, *59*, 519.
[38] X. Zhao, H. Jin, *Int J Heat Mass Transf* **2019**, *133*, 718.
[39] W. H. Lee, C. W. Lee, G. D. Cha, B.-H. Lee, J. H. Jeong, H. Park, J. Heo, M. S. Bootharaju, S.-H. Sunwoo, J. H. Kim, K. H. Ahn, D.-H. Kim, T. Hyeon, *Nat. Nanotechnol.* **2023**, *18*, 754.
[40] G. D. Cha, W. H. Lee, S.-H. Sunwoo, D. Kang, T. Kang, K. W. Cho, M. Kim, O. K. Park, D. Jung, J. Lee, S. H. Choi, T. Hyeon, D.-H. Kim, *ACS Nano* **2022**, *16*, 554.
[41] A. W. Roszak, T. D. Howard, J. Southall, A. T. Gardiner, C. J. Law, N. W. Isaacs, R. J. Cogdell, *Science* **2003**, *302*, 1969.
[42] F. W. Larimer, P. Chain, L. Hauser, J. Lamerdin, S. Malfatti, L. Do, M. L. Land, D. A. Pelletier, J. T. Beatty, A. S. Lang, F. R. Tabita, J. L. Gibson, T. E. Hanson, C. Bobst, J. L. T. Y. Torres, C. Peres, F. H. Harrison, J. Gibson, C. S. Harwood, *Nat. Biotechnol.* **2004**, *22*, 55.
[43] J. B. Mckinlay, C. S. Harwood, *Curr. Opin. Biotechnol.* **2010**, *21*, 244.
[44] K. R. Fixen, Y. Oda, C. S. Harwood, *mBio* **2019**, *10*, e02838.
[45] C. S. Harwood, in *Bioenergy* (Eds: J. D. Wall, C. S. Harwood, A. Demain), ASM, Washington, DC **2008**, pp. 259–271.
[46] K. Alef, D. J. Arp, W. G. Zumft, *Arch. Microbiol.* **1981**, *130*, 138.
[47] H. Yuk, B. Lu, X. Zhao, *Chem. Soc. Rev.* **2019**, *48*, 1642.
[48] N. Huebsch, E. Lippens, K. Lee, M. Mehta, S. T. Koshy, M. C. Darnell, R. M. Desai, C. M. Madl, M. Xu, X. Zhao, O. Chaudhuri, C. Verbeke, W. S. Kim, K. Alim, A. Mammoto, D. E. Ingber, G. N. Duda, D. J. Mooney, *Nat. Mater.* **2015**, *14*, 1269.
[49] C.-H. Li, C. Wang, C. Keplinger, J.-L. Zuo, L. Jin, Y. Sun, P. Zheng, Y. Cao, F. Lissel, C. Linder, X.-Z. You, Z. Bao, *Nat. Chem.* **2016**, *8*, 618.
[50] H. Wu, G. Yu, L. Pan, N. Liu, M. T. Mcdowell, Z. Bao, Y. Cui, *Nat. Commun.* **2013**, *4*, 1943.
[51] D. Jung, C. Lim, H. J. Shim, Y. Kim, C. Park, J. Jung, S. I. Han, S.-H. Sunwoo, K. W. Cho, G. D. Cha, D. C. Kim, J. H. Koo, J. H. Kim, T. Hyeon, D.-H. Kim, *Science* **2021**, *373*, 1022.
[52] J. B. Mckinlay, C. S. Harwood, *Proc. Natl. Acad. Sci. USA* **2010**, *107*, 11669.
[53] M. Bekker, S. De Vries, A. Ter Beek, K. J. Hellingwerf, M. J. T. De Mattos, *J. Bacteriol.* **2009**, *191*, 5510.
[54] V. V. Ramana, S. K. Chakravarthy, P. S. Raj, B. V. Kumar, E. Shobha, E. V. V. Ramaprasad, C. Sasikala, C. V. Ramana, *Int. J. Syst. Evol. Microbiol.* **2012**, *62*, 1790.
[55] J. P. Delong, J. G. Okie, M. E. Moses, R. M. Sibly, J. H. Brown, *Proc Natl Acad Sci U S A* **2010**, *107*, 12941.
[56] B. Atkinson, F. Mavituna, *Biochemical Engineering and Biotechnology Handbook*, Nature Press, New York, NY **1982**.
[57] J. B. McKinlay, C. S. Harwood, *mBio* **2011**, *2*, e00323.
[58] Y. Oda, S. K. Samanta, F. E. Rey, L. Wu, X. Liu, T. Yan, J. Zhou, C. S. Harwood, *J. Bacteriol.* **2005**, *187*, 7784.
[59] E. C. Ziegelhoffer, T. J. Donohue, *Nat. Rev. Microbiol.* **2009**, *7*, 856.
[60] K. K. Henry, W. Ross, K. S. Myers, K. C. Lemmer, J. M. Vera, R. Landick, T. J. Donohue, R. L. Gourse, *Proc. Natl. Acad. Sci. USA* **2020**, *117*, 29658.
[61] D. Kang, H.-I. Ham, S.-H. Lee, Y.-J. Cho, Y.-R. Kim, C.-K. Yoon, Y.-J. Seok, *Environ. Microbiol.* **2021**, *23*, 4726.
[62] S. Sillankorva, P. Neubauer, J. Azeredo, *BMC Biotechnol.* **2008**, *8*, 79.
[63] T. Tatusova, M. Dicuccio, A. Badretdin, V. Chetvernin, E. P. Nawrocki, L. Zaslavsky, A. Lomsadze, K. D. Pruitt, M. Borodovsky, J. Ostell, *Nucleic Acids Res.* **2016**, *44*, 6614.
[64] W. Ding, F. Baumdicker, R. A. Neher, *Nucleic Acids Res.* **2018**, *46*, e5.
[65] C.-K. Yoon, D. Kang, M.-K. Kim, Y.-J. Seok, *Nucleic Acids Res.* **2021**, *49*, 1397.